

The Heidelberg InfraRed Optical Cluster Survey (HIROCS)

I. Layout, instrumentation, and data analysis[★]

H.-J. Röser¹, H. Hippelein¹, C. Wolf², M. Zatloukal¹, and S. Falter¹

¹ Max-Planck-Institut für Astronomie, Königstuhl 17, 69117 Heidelberg, Germany
e-mail: roeser@mpia-hd.mpg.de

² University of Oxford, Department of Physics, Denys Wilkinson Building, Keble Road, Oxford OX1 3RH, UK

Received 6 May 2009 / Accepted 7 November 2009

ABSTRACT

Aims. We describe a survey for distant clusters of galaxies that identified clusters as local overdensities in the 3D galaxy distribution. **Methods.** Optical and near-IR imaging in *B*, *R*, *i*, *z*, and *H* are used to derive photometric redshifts for objects as faint as $m^* + 1$ at a redshift of 1.5. We outline the astrometric and photometric data reduction. The 3D cluster search, based on the photometric redshifts, is described.

Results. On the basis of the first fully reduced 1 square degree of data, we demonstrate that the objectives of HIROCS have been achieved. Four representative clusters from the list of candidates are presented.

Key words. galaxies: clusters: general – surveys – methods: data analysis

1. Introduction

Two important focuses of extragalactic research are the understandings of the large-scale structure in the universe as well as the formation and evolution of galaxies. Studies of clusters of galaxies play a central role in both studies. Clusters are the largest bound entities in the universe and assuming that galaxies in a given cluster have similar evolutionary histories, they provide ideal laboratories for studying galaxy evolution. We know from the seminal work of Butcher & Oemler (1984) that galaxy populations in clusters have evolved significantly until recently because the fraction of blue galaxies in rich clusters increases steadily up to redshifts of about 0.5. Studies of the Butcher-Oemler effect at higher redshifts are more scarce (van Dokkum et al. 2000; Andreon et al. 2004). HST observations have shown that these blue galaxies are usually irregular and merger galaxies (Dressler et al. 1997; Oemler et al. 1997). Furthermore, ground-based IR data show that the population of early-type galaxies is already in place at a redshift of about unity (de Propris et al. 1999; Blakeslee et al. 2003). Studies of clusters of galaxies at higher redshifts will therefore enable us to look back into the childhood of clusters and their galaxies and follow their evolution by comparison with counterparts at lower redshifts. Cosmological models predict the time and length scales of structure formation in the universe. In a model with high matter density Ω_m , no rich clusters are expected to exist at high redshift (Borgani & Guzzo 2001; Voit 2005). The very existence of clusters at redshift >0.8 (Stanford et al. 2005) already infers a low value of Ω_m . The evolution of the cluster population beyond a redshift of 0.3 reported by the ROSAT NEP survey

provides important constraints of models of large-scale structure formation (Gioia et al. 2001). A crucial test will be the analysis of the cluster space density and mass distribution as a function of redshift. Since X-ray selected cluster samples are not expected to increase in size significantly with currently available telescopes (except in the case of serendipitous detections, Rosati et al. 2002), one has to resort to other means for finding clusters at high redshift. Furthermore, the X-ray properties of very distant clusters are currently unknown. It is expected that very young clusters do not yet have a hot intercluster medium and are thus undetectable in X-rays. It is clearly important to detect clusters at redshifts as high as possible. To continue these searches to higher redshift, optical surveys have been performed over the last decade: PDCS (Postman et al. 1996), EIS (Scodreggio et al. 1999), TRCS (Gladders & Yee 2000), LCDCS (Gonzalez et al. 2001), and MUNICS (Drory et al. 2001). None of these surveys has, however, identified a significant sample of clusters with redshifts well beyond 1 (for a summary see Ramella et al. 2000), because only optical and not infrared data (exception Drory et al. 2001) were available, and at $z = 1.5$ the 4000 Å-break, the most important diagnostic feature, is shifted beyond the CCD band-pass into the near-infrared wavelength range. The advent of large IR detectors as well as the *Spitzer* Space Telescope have changed this situation dramatically. Several groups now use these new facilities to extend previous surveys to higher redshift limits. The FLAMINGOS Extragalactic Survey (Elston et al. 2006), for instance, will cover 10 square degrees in *J* and *Ks*, part of which is located in the area of the NOAO Deep Wide-Field Survey. A major breakthrough is expected from the “UKIRT Infrared Deep Sky Survey” (UKIDSS), which has already published its first list of high-redshift cluster detections (van Breukelen et al. 2006, 2007). Eisenhardt et al. (2008) present first results from the IRAC shallow survey with *Spitzer*, which detected 106 candidates beyond a redshift of 1, twelve of which were spectroscopically confirmed.

[★] Based on observations collected at the Centro Astronómico Hispano Alemán (CAHA) at Calar Alto, operated jointly by the Max-Planck Institut für Astronomie and the Instituto de Astrofísica de Andalucía (CSIC) and on observations collected at the European Southern Observatory, Chile, during Max-Planck-time.

In this context, the Heidelberg InfraRed/Optical Cluster Survey (HIROCS) started in 2002, which aims to establish a sizeable sample of distant clusters for studies of the evolution of their galaxy population. As part of HIROCS, we have supplemented the public COSMOS data with H -band observations at Calar Alto and isolated 11 clusters with $z > 1$ (Zatloukal et al. 2007).

Here we describe the layout of the HIROCS survey, the instrumentation used, and its data reduction and analysis. Some results from the reduction of the first square degree are presented to demonstrate the feasibility of the project. In a subsequent paper, we will present the cluster catalogues from all fields together with an assessment of the cluster selection function. This will then allow a detailed discussion of the results. Derivation of the selection function for the 5-filter HIROCS data sets will follow the lines described by Zatloukal et al. (2009), who derived the selection function for the cluster search in the COSMOS field based on the analysis of 10 filters (Zatloukal et al. 2007).

2. Layout of HIROCS

Following the successful application of photometric redshifts in CADIS (Meisenheimer et al. 1998) and COMBO-17 (Wolf et al. 2003), the cluster search was planned based extensively on these methods. However, because of the much larger area to be surveyed (see below), a restriction in the number of filters was inevitable. Furthermore, as HIROCS should find clusters out to redshifts of 1.5, the inclusion of a near-infrared band was mandatory (see above).

2.1. Filter set

To determine the optimum filter selection, a CADIS data set was taken and the number of filters was restricted to the broad-band B , R , and medium-band $i1$ and $i2$ (Röser et al. 2004). The Y and J bands were simulated for all objects, based on the full CADIS data set, from the template library. A multi-colour classification was then performed on this set of 6 filters for objects securely classified as galaxies in the full CADIS data set. For about 1/3 of the galaxies, no photometric redshift with reasonable accuracy ($\sigma_z/(1+z) \leq 0.1$) could be assigned with 6 filters only. The restricted filter set fails completely for redshifts below about 0.7. However, at higher redshift the redshift errors are expected to be ≤ 0.075 . A cluster candidate found in the original CADIS data set was indeed recovered in the reduced filter set. Furthermore, the simulation showed that the results are not seriously affected by omitting the Y -filter. The filter set for HIROCS was thus chosen to consist of broad-band B and R , SDSS i and z , and 2MASS H . The H -band was selected instead of J , because this offers the opportunity to identify clusters at redshifts above 1.5, where J is no longer beyond the 4000 Å-break.

2.2. Targeted limiting magnitudes

The required limiting magnitudes were calculated based on the spectrum of an elliptical galaxy at redshift 1.5. Its spectrum was chosen from the COMBO-17 template library to closely match the colours of the highest redshift ellipticals ($z \approx 1.1$) found in the COMBO-17 survey. Therefore, no evolutionary correction was applied. The absolute B -band magnitude¹ of an L^* -galaxy was also extrapolated from COMBO-17

Table 1. Targeted limiting magnitudes (Vega) and exposure times.

	M^*	K-corr	M^*	obsLim	Δt obs	$\Delta t/\square^\circ$
B	-22.00	1.06	24.2	25.2	10 ks	40 ks
R	-23.09	1.73	23.8	24.8	4 ks	16 ks
i	-23.45	1.42	23.1	24.1	4 ks	16 k
z	-23.79	1.10	22.4	23.4	10 ks	40 ks
H	-25.02	-0.26	19.9	20.9	3 ks	48 ks

(Bell et al. 2004) as $M_B = -22^{\text{mag}}$. We used our own exposure time calculator, integrating the photon flux and exploiting our knowledge of instrumental efficiencies and atmospheric properties (HITRAN 2005). The aim of HIROCS of detecting a galaxy 1^{mag} fainter than L^* to a redshift of 1.5 thus determined the limiting magnitudes given in Table 1.

From Table 1, it follows that – including the overhead for telescope movements and detector read-out – a total of 7.6 clear nights at the 3.5 m-telescope is needed to cover one square degree in all filters.

2.3. Selection of fields

The main science objective of HIROCS is to study the evolutionary effects of the cluster galaxy population. Thus, at least two redshift bins and for a 5σ -effect at least 25 clusters per bin are needed. Therefore, the survey area must ensure the detection of at least 50 clusters at redshifts above 1. Bartelmann & White (2002) considered the number of clusters to be expected in SDSS using the surface-brightness fluctuation method. In SDSS, they expected more than 5 clusters per square degree with redshifts above unity and a mass greater than $5 \times 10^{13} h^{-1} M_\odot$. Based on this, a total survey area of 11 square degrees was initially selected in fields that *i*) are located mainly near the equator for follow-up observations from both hemispheres; *ii*) are devoid of stars brighter than about 9^{mag} ; and *iii*) contain as many objects as possible with spectroscopic redshifts. The latter condition is fulfilled by the CADIS-16h – and the MUNICS-S2F1 field. To exploit the public multi-frequency data, the COSMOS field was also included. So only one field was chosen particularly for HIROCS filling the gap in RA between the 16 h – and the 3 h – fields at RA = 22 h. To cover large-scale structure features such as voids and sheets, the survey areas were originally arranged in strips of $1^\circ \times 3^\circ$, except for COSMOS. Table 2 summarises the data for these fields.

Observations were delayed considerably by instrumental problems and weather losses. After 5 years of observations, it was evident that the total area of HIROCS had to be reduced to finish the survey within a reasonable time. It was decided to restrict the survey area for each field to $1^\circ \times 2^\circ$. So in the end HIROCS now covers $6\square^\circ$ in addition to the COSMOS field.

2.4. Observations

Optical data in B , R , i , and z were collected with LAICA at the prime-focus of the Calar Alto 3.5 m-telescope. LAICA has 4 CCDs with $4\text{ k} \times 4\text{ k}$ pixels arranged in a matrix with a gap somewhat smaller than the area covered by a single CCD. In addition, we used the Wide-Field-Imager (WFI) at the 2.2 m-telescope on La Silla during MPG-time to obtain B and R images. Pixel size is $0''.225$ for LAICA and $0''.238$ for WFI. Typical integration times were 500 s in all filters. For both instruments, 4 pointings were required to cover one square degree contiguously. For each pointing, a short (~ 20 s) exposure was taken in which

¹ We use $H_0 = 72 \text{ km s}^{-1} \text{ Mpc}^{-1}$ and $\Omega_m = 0.3$ and $\Omega_\Lambda = 0.7$.

Table 2. HIROCS fields. Only part of the COSMOS-field is covered by HIROCS (see [Zatloukal et al. 2007](#)).

Field name	RA (J2000)	Dec (J2000)	b	Size	$E(B - V)$
MUNICS-S2F1	03 ^h 06 ^m 12 ^s .0	−0°20′35″	−48°	2° × 1°	0.070 ^{mag}
COSMOS-10h	10 ^h 00 ^m 28 ^s .6	+2°12′21″	+42°	1.4° × 1.4°	0.018 ^{mag}
CADIS-16h	16 ^h 24 ^m 32 ^s .0	+55°44′32″	+42°	2° × 1°	0.006 ^{mag}
HIROCS-22h	21 ^h 59 ^m 58 ^s .7	+2°23′14″	−39°	2° × 1°	0.065 ^{mag}

reference stars were not saturated. To facilitate relative calibration of the mosaic tiles, a short integration offset by half the field size in both coordinates was taken in each filter. To perform flat fielding, twilight flats were acquired and used. The H -band data were collected using only OMEGA2000 ([Bailer-Jones et al. 2000](#); [Kovács et al. 2004](#)), mounted at the prime focus of the Calar Alto 3.5 m-telescope. A pixel of the HAWAII2-detector projects to 0′.45 on the sky, so 15′.4 × 15′.4 are covered by a single exposure. To cover a complete square degree, sixteen pointings are required. Again a mosaic of 3 × 3 images, offset by half the field size of OMEGA2000 was taken to perform a relative calibration of each 1 square-degree mosaic. The NIR flat-fields were constructed from science frames. Bad pixels were isolated in a series of dome flats of increasing exposure time as pixels showing a non-linear behaviour with exposure time. They were treated in the same way as cosmic ray hits.

For absolute spectrophotometric calibration, we measured 8 standard stars in each 1□° mosaic of the HIROCS fields with CAFOS at the 2.2 m-telescope on Calar Alto. These standard stars were selected from USNO and SDSS and had magnitudes of between 15 and 17 in B . Two gratings covered the blue and green part of the spectrum, respectively, with a resolution of 0.46 nm/pixel. The slit width was 4′.5.

Observations started in July 2002 with LAICA, in December 2002 with WFI, and in September 2003 with OMEGA2000. By August 2008, data collection was complete.

3. Data reduction

All data were reduced within MIDAS, the ESO data reduction package, utilizing especially the MIDAS table system for photometry and object classification. Object lists were created with SourceExtractor ([Bertin & Arnouts 1996](#)). For the photometric calibration, 2MASS ([Skrutskie et al. 2006](#)) and SDSS ([York et al. 2000](#)) were also used.

3.1. Optical data

3.1.1. LAICA's optical distortion

The optical distortion of the K3-corrector used with LAICA was measured from one of the survey images of the 3 h-field with respect to SDSS positions for stars. No correction for proper motion was applied. The analysis was complicated by there being no detector at the position of the optical axis.

In the flatfield-corrected images objects were located with SourceExtractor and the coordinates were correlated with SDSS gnomonic coordinates using a distortion model including atmospheric refraction. The free parameters for the model are *i*) the pointing centre of the image; *ii*) the geometric location (shift, rotation, scale) of each detector in the image plane; *iii*) the distortion coefficients (assuming a radially symmetric distortion); and *iv*) the position of the optical axis. These unknowns could not be determined simultaneously but were found iteratively. For

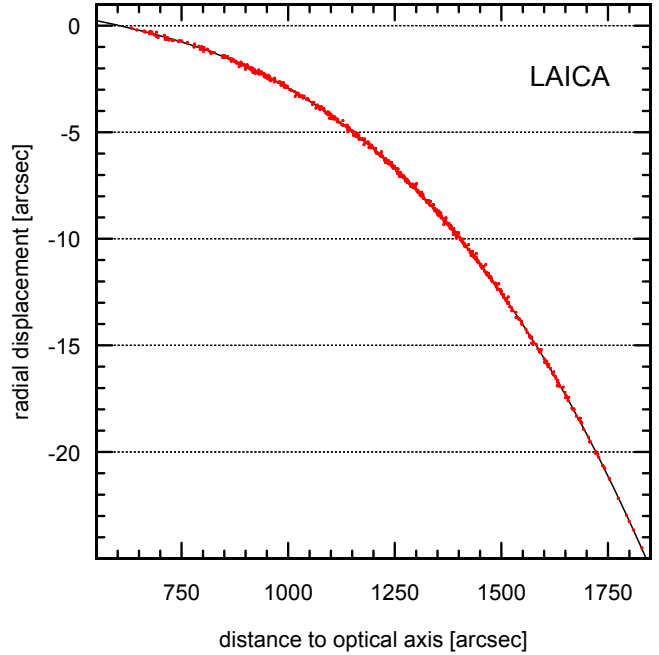


Fig. 1. Optical distortion of LAICA optics measured from an image of the 3h-field. Shown is the radial displacement between the gnomonic SDSS coordinates and the measured position as a function of the distance to the optical axis.

approximate detector locations and zero distortion, the pointing centre in RA and Dec was first determined. The position of each detector in the focal plane was then fitted individually. Deviations between the catalogue and the measured positions were then modelled with a polynomial as a function of the distance to the optical axis. The accuracies of the detector positions were then improved and the entire procedure repeated until a stable solution was found for all 4 detectors. The final rms between the catalogue and the measured positions was 0′.06 in both axes. The maximum distortion at the corners of the field of view is 25″ (see Fig. 1). This distortion is so large that dithered images cannot be aligned with sufficient accuracy, e.g., to construct a median image for cosmic-ray event removal (see below).

Based on this knowledge, the astrometric solution of each image was obtained in three steps. First, all (real) sources with a signal-to-noise ratio (S/N) greater than three were located and the brightest ≤300 per detector field were selected. Second, the positions in the object list were corrected for the (known) distortion. Third, a *linear* fit was applied between the object positions and a survey catalog, such as SDSS or others with object positions gnomonically projected onto the pointing centre of the HIROCS field. Here, the only indispensable parameters were the observing position (required accuracy ∼1′) and the approximate position angle of the instrument. Based on these parameters, the software found matching pairs of observed and catalog objects and thus determined the exact pointing centre and

position angle, scale, shift, and shear for each detector of the mosaic individually.

There are several advantages of this method over using high-order polynomial fits in X and Y :

- the high order – and the accuracy – required to reproduce the distortion correction (6th order) cannot be achieved by low-order polynomials. This is especially important for large fields with high distortion in their outer areas such as for LAICA;
- the distortion correction is radially symmetric. Uneven powers of r (r^3 and r^5) cannot be realized by polynomial fits in X and Y ;
- after the distortion correction, the *linear* fit includes in total only six coefficients (shift, scale, rotation, and shear). Thus, intrinsic positional errors of the reference catalog average out and do not lead to local sinks in astrometric accuracy, which can happen when using e.g., 3rd order polynomials in X and Y with a total of 20 coefficients (note that the positional errors for individual objects are on the order of $0''.1$ for SDSS and UCAC and up to $0''.3$ for USNO and 2MASS). Using more than 100 sources, the linear fit can yield a relative positional accuracy as low as $0''.03$, distortion correction and measurement errors being included;
- the astrometry is extremely fast. The astrometric solution for a $4\text{ k} \times 4\text{ k}$ image is obtained within 10 s, including object search and distortion correction.

For very large detector fields and low telescope elevations, the non-linear elevation dependence of the differential atmospheric refraction leads to small systematic errors when using a linear fit. The positional errors therefore vary by $\pm 0''.02$ within 1° along the meridian ($h = 30^\circ$).

3.1.2. LAICA fringes

Both LAICA and WFI data are affected significantly by fringing at near-IR wavelengths because of the interference of night-sky emission lines within the CCD. This was the original reason why the use of WFI was restricted to shorter wavelengths only. However, the fringing of LAICA was equally strong. In addition LAICA suffers from electronic instabilities.

Before correcting the fringes, each image needed to be flattened over large scales by a smoothing length longer than the typical distance between the fringes. To derive a measure of the fringe strength, each image was rebinned with a step size of about ten times the original step size, thus reducing the pixel-to-pixel variation to about a tenth. Bright stars were masked with the mask size depending on the brightness of the star. A histogram of all unmasked pixel values was produced and from its central part two quantities were derived: the background level could be seen in the mean level, and the fringe strength and the remaining pixel-to-pixel variation together determined the full width at half maximum. The pure fringe strength was thus given by

$$= \frac{\sqrt{(\text{FWHM_histo})^2 - (\text{pix_to_pix_var})^2}}{\text{background level}}.$$

Not all photons contributing to the background level also contribute to the strength of the fringe pattern (e.g., moonlight as a continuum source does not). The fringe strength derived above was used to determine empirically the “fringing” fraction of the background level. A fringe pattern was then derived as a kappa-sigma-clipped sum (to remove cosmic-ray hits and residuals of

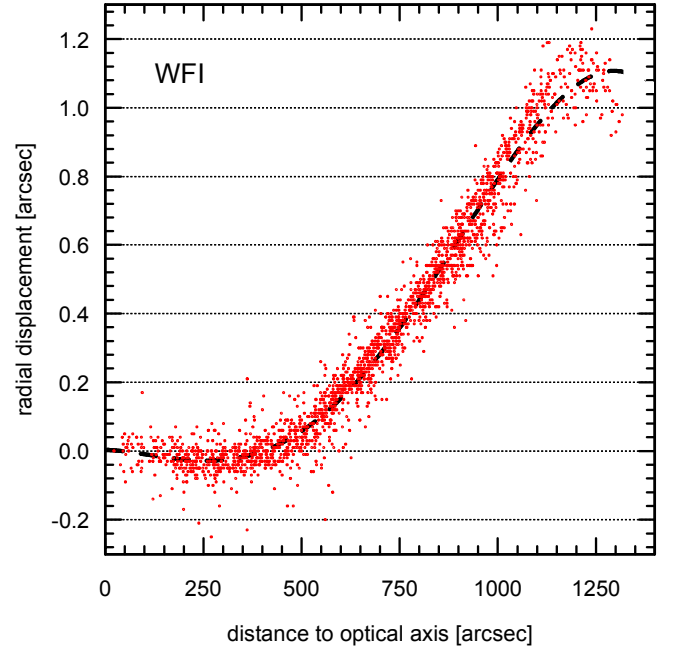


Fig. 2. Optical distortion of the Wide-Field-Imager measured from an archival image of M 67 and coordinates from SDSS.

stars) over all dithered science frames. Using the frame-specific fringing strength, this final fringe pattern was then scaled to each individual frame and subtracted to remove the fringes.

For filters including two or more strong atmospheric emission features (mostly OH bands), the above correction often does not provide satisfactory results: the relative strength of the atmospheric emission bands changes during the night, thus leading to an overcorrection of one band and an undercorrection of another in various science frames. In the case of two major bands such as in Gunn z , an iterative procedure was able to remove these remaining over- and under-corrected fringes. For this, the science frames were separated into two groups. One group contained the frames in which the fringes due to the first band were over-corrected and under-corrected because of the second band. In the other group, the fringe behaviour was vice-versa. To derive the fringe pattern for the second-order correction, the fringe amplitude of the second group had to be reversed before averaging all frames. For frames with a fringe strength below a threshold level, no second iteration was performed.

3.1.3. WFI's optical distortion

The distortion of the WFI optics was determined from a V-band image of M 67 retrieved from the ESO archive (WFI.2004-02-12T04:19:54.648.fits). The procedure was identical to that used for LAICA. The final rms values between the catalogue and the measured positions were $0''.06$ in X and $0''.05$ in Y . The maximum distortion at the corners of the field of view is $1''.1$ (Fig. 2).

3.1.4. WFI bad columns

The Wide-Field-Imager CCDs have many bad columns, though most of them can be simply corrected with an additive offset. Internal flat-field series taken weekly during the instrumental health checks were used to analyse the bad columns. These series are taken with exposure times between 2.1 and 300 s, corresponding to a count level of ~ 700 counts to saturation. For each

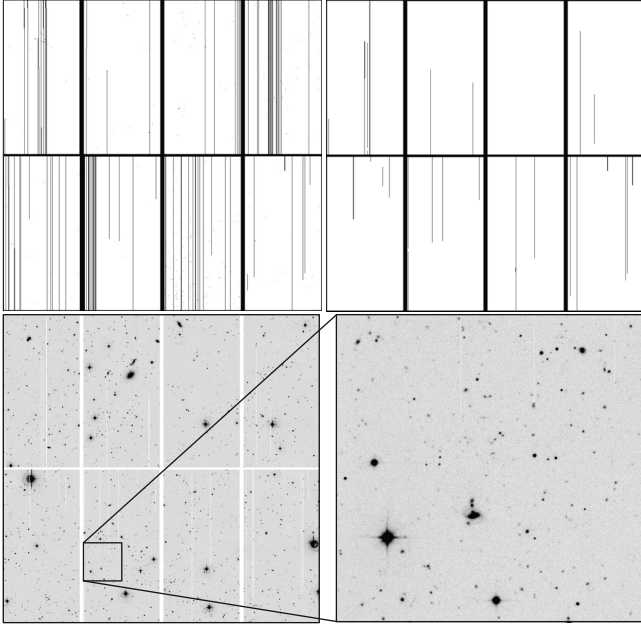


Fig. 3. Correction of bad columns in WFI images. *Upper left:* all bad columns (gaps between detectors are marked in solid black). *Upper right:* bad columns, that cannot be corrected for, which are far fewer in number. *Lower left:* example of a reduced image with remaining bad columns indicated in white. *Lower right:* zoomed image of reduced frame demonstrates the quality of the bad-column correction.

pixel, the level was fitted as a function of exposure time with a straight line. Originally, this analysis aimed to identify bad pixels, which by definition are those, for which the exposure level does not depend linearly on exposure time. However, a map of the zero-order coefficients of these fits exhibited a general offset over the whole field (probably because of a slight non-linearity) and superimposed the bad columns, most of which showed a constant offset on the general background. From these, a map of column offsets was derived, which was subtracted from all raw images (Fig. 3).

We note that the correction of bad columns directly assesses the S/N achievable in a given exposure time because each bad column results in the loss of data in a stripe of width of the aperture used in photometry, typically on the order of $3''$.

3.2. Near-IR data

Basic reduction of the OMEGA2000 data (flatfielding, sky subtraction) used the upgraded pipeline originally written for a quick-look reduction at the telescope (Faßbender 2003). The upgrade includes two passes, where objects detected in the summed image of the first pass are masked before the construction of the sky background map in the second pass (Faßbender 2007). Summation is performed on a sub-pixel grid by rebinning to the original pixel size only the output image using weights derived from the relative transmission, seeing, and background values (Gabasch et al. 2008). Since the multiplicative flat-field showed uncorrectable temporary variations (i.e., the level at which the photon limit in the background noise was reached often varied systematically throughout a night by several tens of percent), the original sky images delivered by the pipeline were not used directly. The sky images were instead smoothed by a median over 50×50 pixels before subtraction. In this way remaining flat-field features were not *subtracted* out. Since the uncertainty in

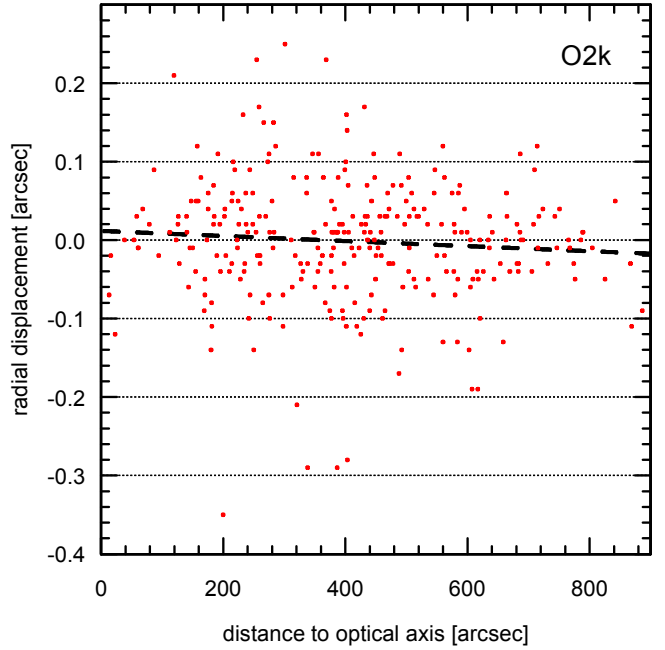


Fig. 4. Optical distortion of O2k measured from an M67 image and coordinates from SDSS.

each flux measurement is derived from the background noise in each frame, subtraction of the unsmoothed sky would have led to unrealistically small photometric errors. Sub-sums of 5 single 1 min exposures were finally created, to reduce the total number of images in the photometric analysis (see below). The optical distortion of OMEGA2000 is negligible (Fig. 4).

3.3. Straylight correction

Instruments with optics consisting of several lenses such as those used in the present project tend to produce scattered light with varying intensity from objects and night sky all over the field. This scattered light is also present in flatfield exposures and in general cannot be disentangled from the “real” flatfield illumination. If an image is corrected with this “distorted” flatfield, the background may become flat but the photometry of the objects will be inaccurate. To avoid this, the scattered light was assumed to be radially symmetric around the optical axis. The deviation between the magnitude derived from the full photometric reduction and the SDSS or 2MASS magnitude for well measured stars was averaged in radial rings and fitted as a function of distance to the optical axis with segmented polynomials. The polynomials were then used to correct the measured count rates and the entire photometric calibration was repeated. Figure 5 gives representative examples of these corrections for all three instruments. For each observing campaign and filter, only one flatfield was constructed, usually from the highest quality twilight flatfield exposures. Thus, the above analysis could be applied to all images in a given filter during a given campaign. There were substantial variations from campaign to campaign, which reflected the different quality of the twilight flats obtained. This contradicts the assumption of a constant straylight correction as suggested by Manfroid et al. (2001) or Koch et al. (2004).

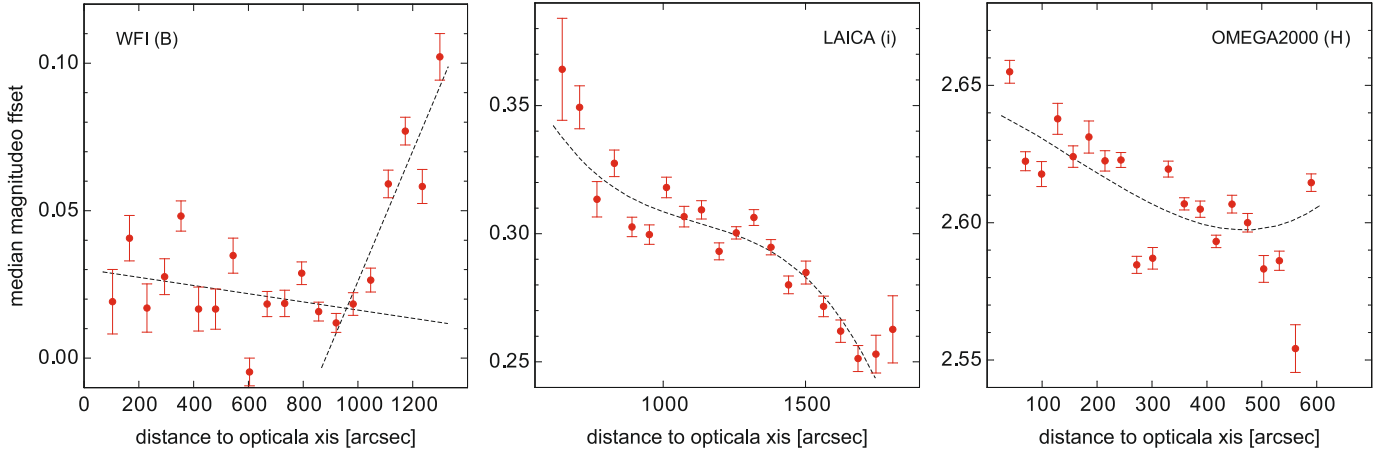


Fig. 5. Straylight correction in magnitudes for WFI in *B* (left), LAICA in *i* (centre) and OMEGA2000 in *H* (right). Straylight corrections typically amount up to 0.1^{mag} for LAICA and WFI and are almost negligible in OMEGA2000.

4. Data analysis

4.1. Master list of objects

In multi-colour surveys, a master list of objects has to be made from detections in all different filters. While such a list can be obtained by searching the individual sum frames for each filter and merging the lists afterwards, we proceed as follows. Each single frame was resampled into a frame according to the gnomonic projection for one square degree with a common pointing centre following a modification² of the drizzle algorithm (Fruchter & Hook 2002). The transformation parameters were derived from the distortion-corrected positions of well-defined stellar images in the field in comparison with SDSS positions as described above (typical rms for OMEGA2000 and WFI was 0''.05 and 0''.07, respectively). These gnomonic images were first combined into a median frame, which was used to detect cosmic-ray events. Pixels affected were replaced by the scaled median and the replaced pixels were traced back to the original (unrebinned) image and also replaced there. The cosmic-corrected gnomonic images in a given filter were combined to produce a sum frame for each square degree. SourceExtractor (Bertin & Arnouts 1996) was used to create an object list for each of these sum images. The resulting object lists were then used to create an artificial image (still in gnomonic coordinates), objects being added at the positions found by SourceExtractor with shapes as determined by SourceExtractor and with weight proportional to S/N. All objects found in the various filters were entered into the *same* artificial image. In this way, the object positions were averaged over the individual positions as measured in each filter. The objects were located by SourceExtractor with a special setup file appropriate for a noise-free image with zero background. The resulting object list provided the master list of positions, which were projected back onto the flatfield-corrected, cosmic-cleaned single (unrebinned) images for photometry. At the same time, the master list also provided the celestial coordinates right ascension and declination with an accuracy of higher than 0''.05.

² The original drizzle algorithm does not necessarily fill all pixels. The modified version fills all pixels with the value of the nearest pixel in the original image. Thus, the “drizzled” image here is photometrically incorrect, in contrast to the original version.

4.2. Photometry and object classification

The principles of the photometric reduction are given in previous papers (Meisenheimer & Röser 1987; Röser & Meisenheimer 1991; Meisenheimer & Röser 1993) and are identical to the procedure used in the CADIS and COMBO-17 projects (see e.g., Wolf et al. 2003). For a successful multi-colour classification, the *relative* calibration in the various filters is more important than the *absolute* flux calibration, since the classification is performed in colour space. The measurement for a given object in each filter and image has to refer to the same position and the same resolution. The first requirement is fulfilled by our astrometric accuracy (see also Röser & Meisenheimer 1991). For the second issue we derived the instrumental magnitude from a weighted sum over the object image area at the position provided by the master list. This is equivalent to a convolution of a Gaussian weighting function (width σ_{weight}) with the point-spread-function (PSF, width σ_{seeing}) of the image taking only the value at the image position from the convolution. The width of the weighting function was set by the requirement of a common effective beam with width $\sigma_{\text{effective beam}}$ (equivalent to the synthesised beam in aperture synthesis radio astronomy) for all images taken in different seeing conditions, i.e.,

$$\sigma_{\text{effective beam}} = \sqrt{\sigma_{\text{seeing}}^2 + \sigma_{\text{weight}}^2}.$$

This procedure provided a measured count rate for every object in every single frame³. Normalization was performed such that the total flux is recovered for stellar images. As the individual tiles of each mosaic of 1° were imaged in varying observing conditions count rates were scaled as follows. Results for each image in a given filter were combined within a MIDAS table in a block of columns, the highest quality image filling the first block (=normalization block). For each block, a set of clearly defined stellar images was used to calculate a normalization factor for the count rate relative to the normalization block. From thereon, the photometry had to be performed only for the normalization blocks and could then be transformed to the other blocks using the normalization factors. This procedure is more accurate than calibrating each block individually using sky survey data

³ In the case of near-infrared images, sub-sums of typically 5 images were created in which the count rate was measured. This avoided excessively large numbers of input frames due to the short integration times.

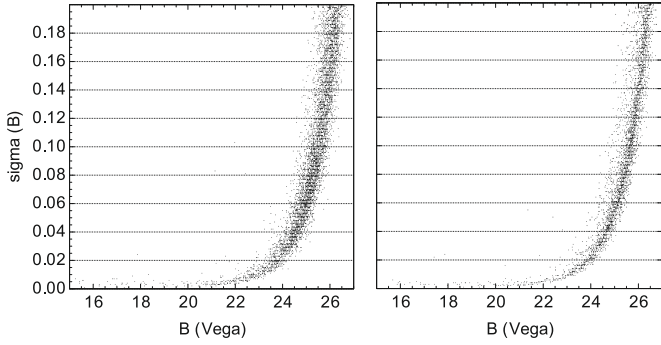


Fig. 6. Error in the B -band magnitude as a function of B -magnitude (Vega) for all tiles of 03hA (*left*, only every 25th data point plotted). The varying depth of the tiles contributes to the spread. The same for a single pointing is shown in the *right panel*, now for every second data point.

because a large number of calibration objects is available even in shallow images. The varying sky transparency between the individual tiles in the mosaic was determined for the normalization blocks by a comparison of magnitudes for well-defined stellar images with 2MASS- and SDSS-magnitudes, providing a “mosaic” correction factor for each tile. Finally, the measured count rates in each block were scaled onto a common *relative* photometric scale using the normalization and mosaic factors.

Absolute calibration was achieved using spectra of 8 stars in each 1° field (see above). Photometric calibration was performed relative to Oke (1990) standards. However, the spectroscopic HIROCS standard stars were only used to visually classify the stellar type by comparison with spectra from a stellar library (Pickles 1998). This best-fit library spectrum was scaled to an absolute flux by integrating over the system response function for SDSS and 2MASS (for details, see Falter 2006). These spectrophotometric standard star spectra were then integrated over the HIROCS filters and the results for all available standard stars in a given mosaic were averaged for the final absolute calibration. Full error propagation was calculated for all these scaling steps. The final result was a MIDAS table (called flux table) holding all available information for each object in the field of the mosaic, including position, flux, and its error.

4.3. Limiting magnitudes achieved and colour accuracies

The 5σ limiting magnitudes were derived as the average magnitude over all objects in a given filter with errors of $(0.2 \pm 0.01)^{\text{mag}}$. An example of the error distribution is given in Fig. 6 for the B -band. The 5σ limiting magnitudes for each filter and tile are shown in Fig. 7.

Since the object classification is performed in colour space, consistency between colours is more important than the absolute flux level. The colours were compared to the locus of the main sequence in colour-colour plots, by plotting the measured colours of stellar objects (according to the SDSS classification) over the locus of the main sequence from the template library (Fig. 8).

Only $i-z$ showed a noticeable offset with respect to the stellar library of 0.04^{mag} . All other colour-colour plots agreed very well with the library to within a few hundredths of a magnitude (see Fig. 8). From this, an accuracy of the colours of $0.02-0.03^{\text{mag}}$ can be deduced.

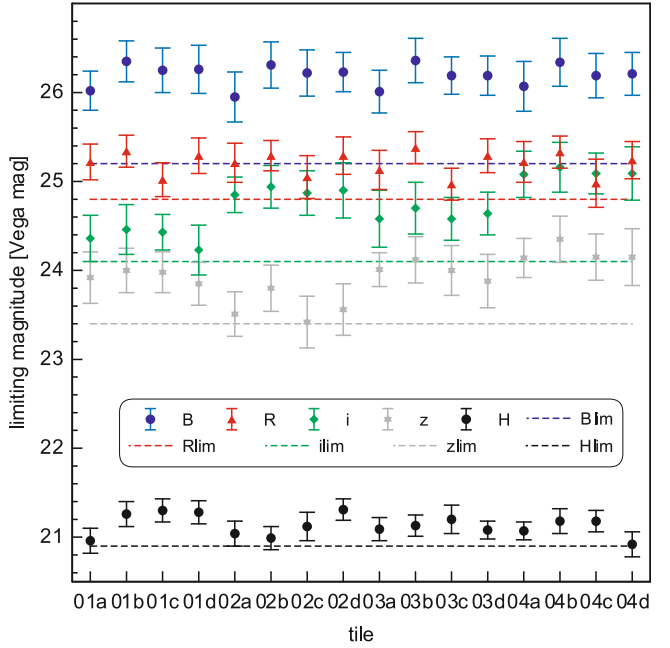


Fig. 7. Limiting magnitudes achieved in each tile of the 03hA-field for each of the 5 filters. Note that WFI tiles 01a, 02a, 03a, 04a, etc. represent one exposure, whereas for LAICA, 01a, 01b, 01c, and 01d etc. are exposed together. Dashed lines indicate the targeted limiting magnitude.

4.4. Accuracy of the photometric redshifts

The flux table was used as input to the object classification procedure described by Wolf et al. (2001, 2004), which determines the Bayesian probabilities for class membership and expectation values for redshifts based on the object colours (photometric redshifts z_{phot}). For the errors in z_{phot} , we use the rms variance of the probability distribution function $p(z)$ in redshift. We do not use all available information about the true $p(z)$ function because we consider its fine-structure shape to be too unreliable.

Ideally one would like to compare the photometric redshifts with a large set of slit spectra for the various galaxy types distributed over the redshift range of interest. The location of the HIROCS 03h-field was chosen to include one of the MUNICS fields (Drory et al. 2001). For this field, slit spectra had been taken by the MUNICS team (Feulner 2004). Unfortunately, in the redshift range of prime interest for HIROCS ($0.5 < z < 1.5$), only 25 well measured objects with positional match superior to $1''$ were found in the catalogue (Fig. 9).

There is only one serious outlier in Fig. 9 in the redshift range of interest. Ignoring the outlier and the data point with a very large error in z_{phot} , the average of $(z_{\text{spec}} - z_{\text{phot}})/(1 + z_{\text{spec}})$ is 0.030 ± 0.022 . A slight trend of the true redshift being underestimated might be discernible. But due to the small number of objects no final conclusion can be drawn.

A second test is provided by the HIROCS analysis of the COSMOS field (Zatloukal et al. 2007). Here spectroscopic redshifts from zCOSMOS as well as photometric redshifts based on 30 filters from the COSMOS team are available (Lilly et al. 2007; Ilbert et al. 2009). The filters provide equivalent wavelength coverage to the 5 HIROCS filters. For comparison, the object catalogue from Zatloukal et al. (2007) was reclassified using only the 5 HIROCS filters. The resulting photometric redshifts agree very well with those used in Zatloukal et al. (2007) except for the region around redshift 1.2 where an increased scatter is evident (Fig. 10). A comparison with the photometric redshifts

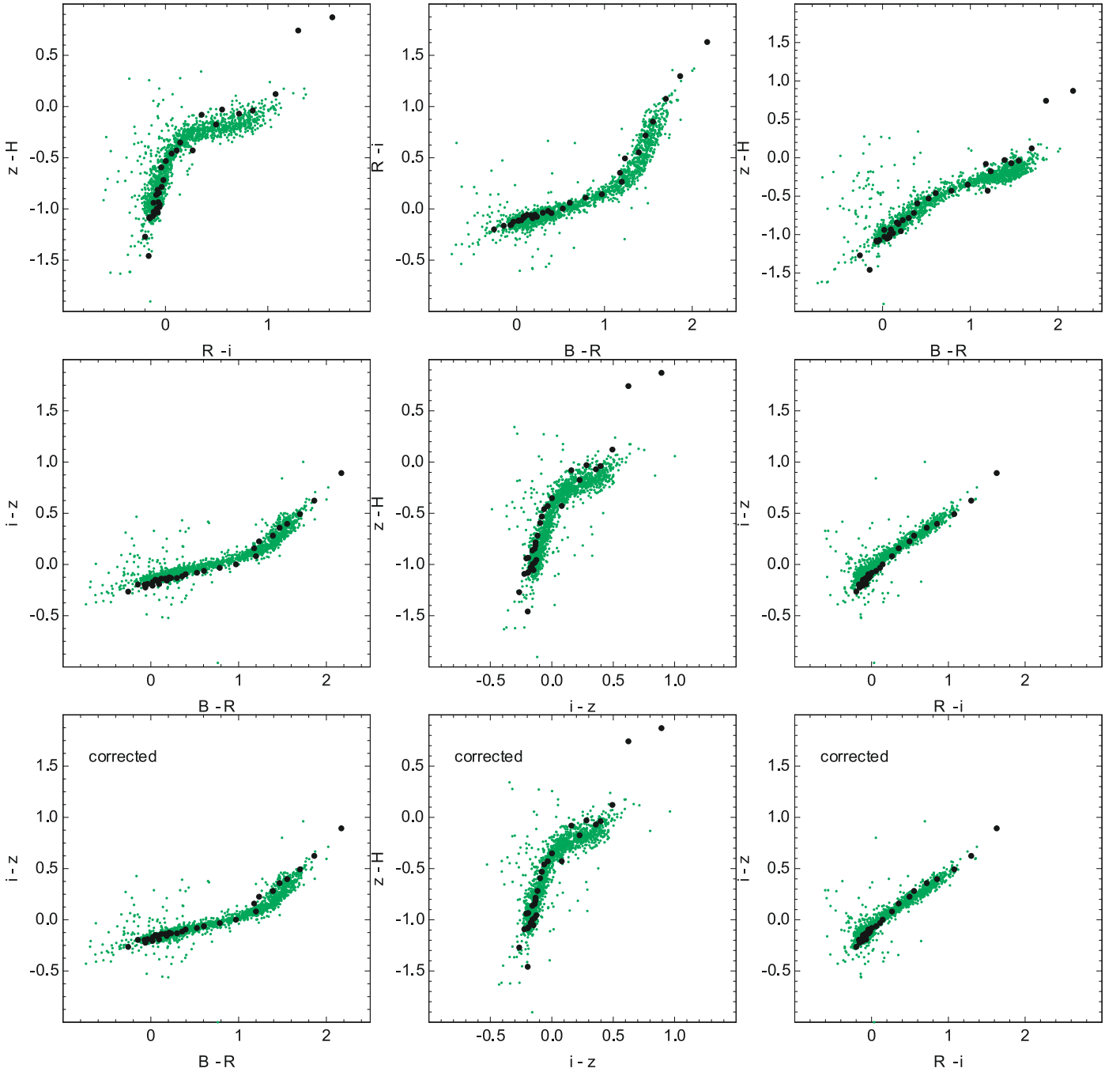


Fig. 8. Locus of stellar objects (green dots) in colour–colour plots. The location of the stars from the template library is outlined by the black dots. Plots involving $i - z$ (central row) do not match perfectly. A colour shift of $i - z = -0.04^{\text{mag}}$ perfectly matches the locus of the stars with the main sequence from the library (bottom row).

from Ilbert et al. for $z > 1$ showed that the HIROCS photometric redshifts are more dispersed for each spike in Ilbert’s redshift histogram over almost the whole range $1 < z < 1.5$. The reason for this effect is currently unknown. A comparison of the 5-filter photometric redshifts with spectroscopic redshifts available from zCOSMOS remains affected by small-number statistics in the range $1 < z < 1.5$ (Fig. 11).

4.5. Calculating rest frame luminosities

Rest-frame colours and luminosities were calculated for each galaxy with a photometric redshift on the basis of the best-fit

library spectrum. From this, the k -correction was calculated from the observed filter closest in wavelength to the redshifted standard filter, for which the absolute magnitude was to be determined. Since our photometry provides total magnitudes only for stellar images, an aperture correction was derived from SourceExtractor’s MAG_BEST. First, the magnitude offset between MAG_BEST and the HIROCS magnitude was determined for unsaturated stars (as classified by SDSS) to an accuracy of 0.15%. This offset was subtracted from all differences between HIROCS-magnitude and MAG_BEST to obtain the aperture correction, which was assumed to be colour independent. This procedure was first applied to the R -band sum image, which worked for more than 80% of the objects. The procedure was then

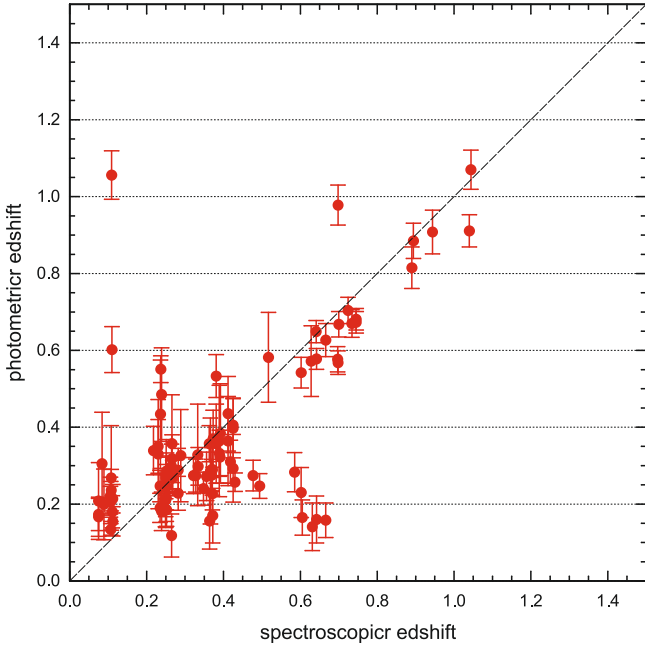


Fig. 9. Comparison of the available spectroscopic redshifts from MUNICS and SDSS with the photometric redshifts.

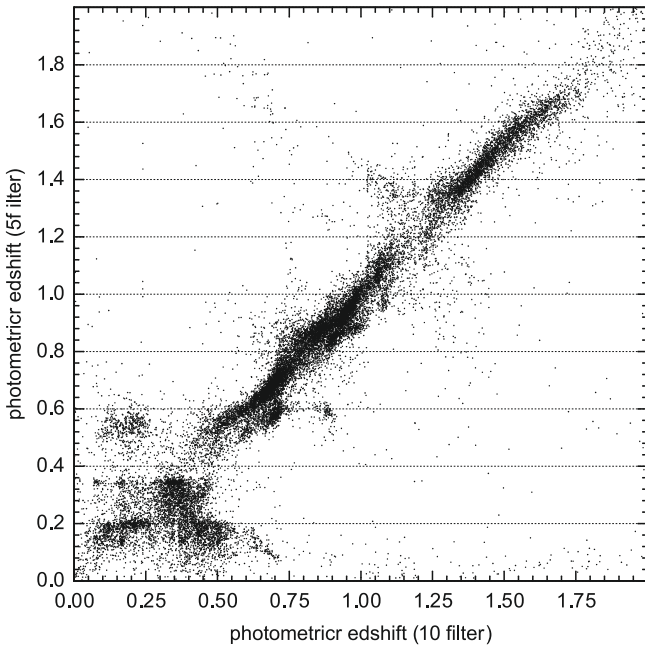


Fig. 10. Comparison of the photometric redshifts based on 10 filters from Zatloukal et al. (2007) with the classification using only the 5 HIROCS filters. The same features as in Fig. 11 are reproduced.

repeated for the B and the H sums, so in the end the aperture correction was available for 97% of the objects.

4.6. Searching for clusters

The basic idea behind the cluster search method is to search for objects living in overdense regions compared to the average 3D object density in the field under investigation (a similar approach was applied by Trevese et al. (2007) to the CDFS).

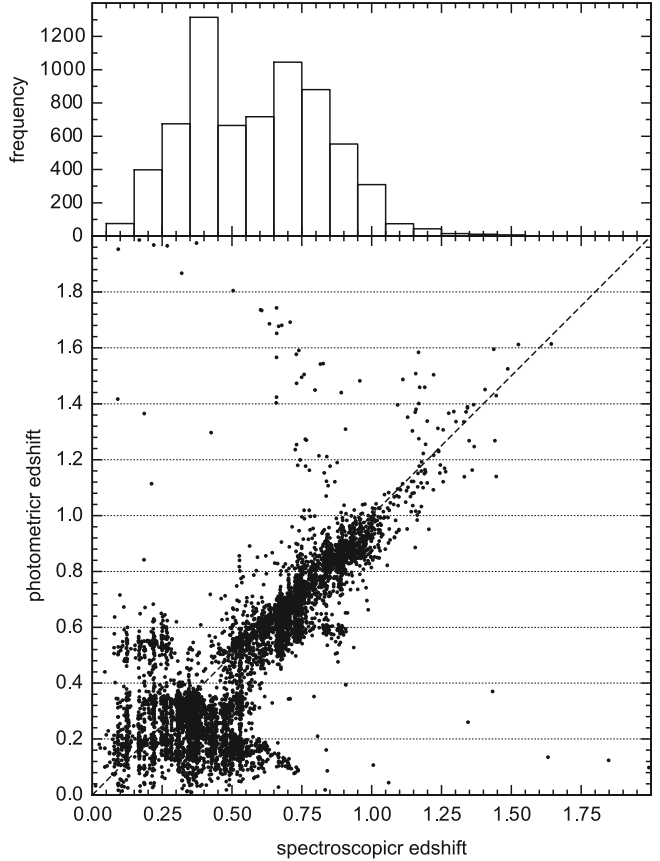


Fig. 11. Spectroscopic redshifts in the COSMOS field compared with the photometric redshifts based on 5 filters and using the 5-filter HIROCS set. The histogram at the top shows the number of objects being drastically reduced beyond a redshift of 1. Below redshifts of about 0.5 photometric redshifts based on only 5 filters cannot be used.

Based on the photometric redshift, the projected Abell radius (or fraction thereof) around any given galaxy on the sky was calculated. The fraction of the probability distribution function contained in the velocity interval $-\beta < v_{\text{rel}} < +\beta$ was determined for each galaxy within this radius on the basis of its photometric redshift and its error (see Fig. 12). These fractions were summed for all objects within the projected Abell-radius and defined the local galaxy density, which was normalized to the average density of galaxies over the whole field at the redshift of the galaxy under consideration. The relative velocity and its uncertainty for a galaxy with redshift z_1 with respect to the galaxy under consideration with redshift z_0 , was calculated to be $v_{\text{rel}} = c \cdot ((1+z_1)^2 - (1+z_0)^2) / ((1+z_1)^2 + (1+z_0)^2)$, which assumes that galaxy 1 is at the same cosmological distance as galaxy 0. The results were rather insensitive to the upper and lower velocity limits, which currently correspond to $\beta = 6000 \text{ km s}^{-1}$. Figure 13 shows the distribution of these densities for the 3hA-field. The cut, which defines objects in an overdense region, was defined by fitting a Gaussian to the rising flank and peak of this distribution. The cut is currently set to be 3σ . A plot of the location of galaxies in overdense regions on the sky highlights cluster candidates as concentrations of overdense objects (Fig. 14).

Friends-of-friends algorithms (FoF) are frequently used in searching for clusters in panoramic data sets (see Botzler (2004) for extensive references and e.g. Li & Yee (2008)). Here an algorithm was developed that operates on the list of *overdense*

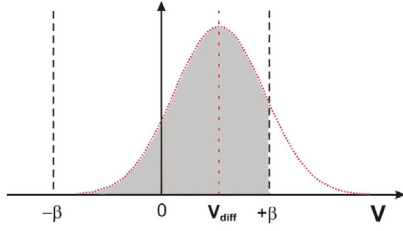


Fig. 12. Calculation of the local overdensity of galaxies from the cumulative distribution function in the interval $\pm\beta$.

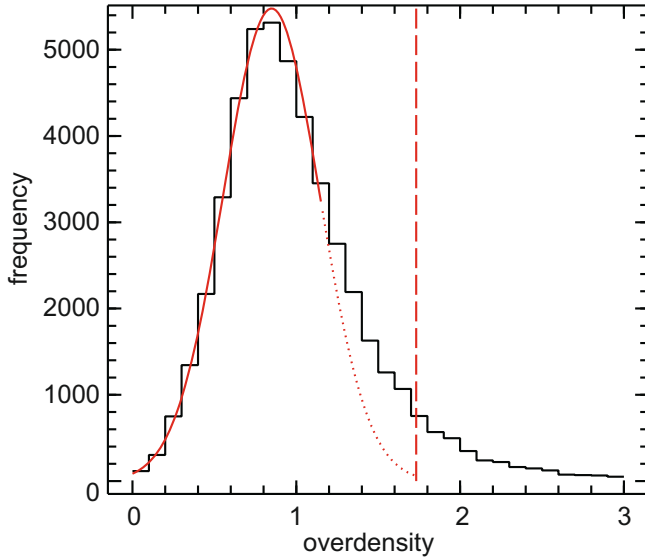


Fig. 13. Distribution of overdensities. A Gaussian was fitted to the rising flank and peak (solid red line) and the 3σ -cut (dashed line) delineates the region where cluster candidates, i.e., galaxies in overdense regions, are to be found.

objects (Zatloukal 2008) sorted with respect to decreasing local density:

- the object with the highest overdensity value is chosen as a starting point;
- the starting object's photometric redshift is not necessarily the mean redshift of the structure. The mean structure redshift is estimated as follows. In a 300 kpc search radius around the most overdense object, the three most overdense objects (including the starting object) within a redshift range of ± 0.1 around the redshift of the most overdense object are selected. Their photometric redshifts are averaged, resulting in the estimated mean redshift of the structure;
- the search cuts in redshifts space are defined to be $\pm 2\sigma$ around the mean redshift. The σ -value is judged from the comparison between the spectroscopic and photometric redshifts of the comparison sample (0.07 was used here);
- all connected overdense objects of the structure are searched with a FoF algorithm. Again, the search radius between galaxies is chosen to be 300 kpc. The friends are indicated in the object table with the structure ID;
- once all members of the structure are found, the algorithm continues from the beginning, this time searching around the most overdense object that has not yet been found to belong to a structure;
- as a last step, a cutoff at a minimum number of objects per structure of 6 was applied. In this way, the inclusion of structures with low significance in the output catalog is avoided.

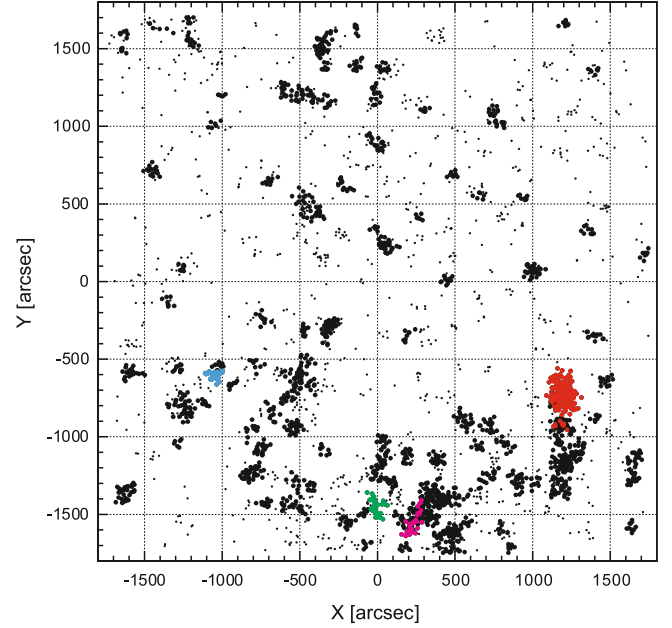


Fig. 14. Galaxies living in overdense regions delineate the location of candidates for clusters of galaxies. Small black dots represent galaxies in overdense regions not allocated to a cluster by the FoF algorithm. Large black dots represent the cluster members. The four cluster examples discussed in the text are marked in colour (red = #1, blue = #6, green = #11, purple = #61). The pointing centre for this gnomonic projection was at RA(J2000) = $3^{\text{h}}6^{\text{m}}12^{\text{s}}.48$ and Dec(J2000) = $-0^{\circ}20'38''$.

Because no assumptions about the shape of the structures and the distribution of the member galaxies enter into this algorithm, it is also capable of reliably selecting structures that are shaped asymmetrically or do not have a strong central concentration. However, because of the FoF selection of member galaxies, it is possible that two structures that are close in redshift space as well as in the projection on the sky are not separated. Furthermore, it is possible that in this case not all member galaxies are selected. If the structures' redshifts are not as close together, the combination of redshift separation, intrinsic scatter, and the $\pm 2\sigma$ redshift boundaries might cause the high and low redshift tails to be truncated, thus reducing the number of selected member galaxies.

The cluster selection algorithm can be configured to only select structures within a specified redshift range by limiting the selection of starting objects to overdense galaxies within these boundaries. We may select massive structures containing many members slightly outside this redshift range, some of their overdense members being included in the search range because of the scatter in the photometric redshifts, serving as starting points for the algorithm. In this case, nearly all of their member objects are selected since the estimate of the average redshift of the structure is the mean value of the overdense object selected initially (with its redshift being within the boundaries), and the two most overdense galaxies within 300 kpc in projection on the sky and close in redshift space (± 0.1 , this time not taking the boundaries into account). The estimated structure redshift might be slightly off because of the bias of the initially selected object, but object selection will still be nearly complete because the redshift boundaries do not affect the subsequent selection of members.

The HIROCS cluster selection based on the local density calculation and overdense object selection using the algorithm described above has been characterized for the COSMOS field with

Table 3. Cluster candidates.

ID	X	Y	RA (J2000)			Dec (J2000)			$\langle z \rangle$	n_{gal}	$M_V(\text{tot})$	n_{gal} $\sigma_z \leq 0.15$	$\langle z \rangle$	
1	1196.0	-736.1	3	4	52.7	-	0	32	55	0.651	175	-25.8	136	0.653
3	331.7	-1430.3	3	5	50.4	-	0	44	29	0.834	61	-25.0	37	0.827
5	1644.4	-1272.7	3	4	22.9	-	0	41	51	1.053	22	-24.2	19	1.046
6	-1054.2	-608.8	3	7	22.8	-	0	30	47	1.112	26	-24.5	14	1.096
7	458.2	-1624.9	3	5	41.9	-	0	47	43	1.194	39	-24.9	23	1.215
9	999.7	71.6	3	5	5.8	-	0	19	27	0.643	34	-24.2	30	0.649
10	1183.0	-941.9	3	4	53.6	-	0	36	20	1.086	38	-24.8	29	1.068
11	-7.7	-1449.3	3	6	13.0	-	0	44	48	1.304	30	-24.9	26	1.315
13	386.6	-1147.2	3	5	46.7	-	0	39	46	0.936	22	-24.3	18	0.938
14	1173.5	-1282.4	3	4	54.2	-	0	42	1	1.326	47	-25.4	34	1.303
15	1138.2	-794.0	3	4	56.6	-	0	33	52	0.909	9	-22.4	6	0.911
16	-533.9	-937.5	3	6	48.1	-	0	36	16	0.620	36	-24.8	26	0.614
17	-1248.8	-812.3	3	7	35.7	-	0	34	11	0.577	45	-24.5	26	0.576
18	210.7	-1516.0	3	5	58.4	-	0	45	54	1.201	37	-25.0	24	1.195
19	-1588.6	-587.7	3	7	58.4	-	0	30	26	0.912	23	-24.2	20	0.909
20	471.3	-1594.5	3	5	41.1	-	0	47	13	1.465	10	-24.2	6	1.437
22	36.2	-1173.4	3	6	10.1	-	0	40	12	1.408	63	-25.8	45	1.388
24	-814.5	-1232.1	3	7	6.8	-	0	41	11	0.597	41	-24.3	30	0.608
25	393.9	-1414.6	3	5	46.2	-	0	44	13	0.560	71	-25.0	55	0.569
26	902.1	-1289.3	3	5	12.3	-	0	42	8	1.244	24	-24.6	19	1.227
27	-4.4	889.0	3	6	12.8	-	0	5	49	1.353	17	-24.6	14	1.330
30	-471.9	-311.9	3	6	43.9	-	0	25	50	1.053	10	-23.4	8	1.067
31	1235.5	-1149.9	3	4	50.1	-	0	39	48	0.658	76	-24.9	60	0.665
33	-1621.1	-1360.8	3	8	0.6	-	0	43	19	0.914	31	-24.4	23	0.904
36	1723.1	175.3	3	4	17.6	-	0	17	43	1.001	8	-23.4	8	1.001
39	-746.8	-1075.6	3	7	2.3	-	0	38	34	0.646	22	-23.2	15	0.659
40	767.5	1055.4	3	5	21.3	-	0	3	3	0.968	25	-24.0	21	0.941
44	-310.0	-297.2	3	6	33.1	-	0	25	36	0.606	34	-24.1	23	0.629
45	-13.8	1209.5	3	6	13.4	-	0	0	29	1.344	17	-24.1	10	1.374
47	-502.9	1196.8	3	6	46.0	-	0	0	42	0.877	31	-24.3	28	0.875
49	57.9	227.4	3	6	8.6	-	0	16	51	0.698	25	-23.8	21	0.699
50	1397.0	-349.8	3	4	39.3	-	0	26	28	0.756	13	-23.3	13	0.756
54	-197.5	-1551.9	3	6	25.6	-	0	46	30	0.577	17	-23.2	12	0.584
56	-90.1	-1491.7	3	6	18.5	-	0	45	30	0.888	10	-23.5	8	0.860
58	1674.6	-1121.1	3	4	20.8	-	0	39	19	0.708	13	-23.5	11	0.704
61	229.7	-1558.3	3	5	57.2	-	0	46	37	1.599	30	-25.2	18	1.598
62	-134.2	1391.2	3	6	21.4	+	0	2	33	1.515	13	-24.5	6	1.519
63	-437.5	480.4	3	6	41.6	-	0	12	38	0.469	32	-34.9	24	0.461
67	1359.5	326.7	3	4	41.8	-	0	15	12	1.393	10	-23.8	8	1.396
69	-1024.3	-548.3	3	7	20.8	-	0	29	47	1.465	11	-24.0	8	1.448
72	-722.2	-1427.7	3	7	0.6	-	0	44	26	0.837	12	-23.3	12	0.837
75	-550.9	-1450.5	3	6	49.2	-	0	44	49	0.883	19	-23.7	15	0.906
77	560.9	-893.7	3	5	35.1	-	0	35	32	0.636	24	-23.4	24	0.636
78	266.8	414.5	3	5	54.7	-	0	13	44	0.592	7	-22.5	7	0.592
79	-1257.1	92.0	3	7	36.3	-	0	19	6	1.631	7	-23.5	6	1.596
81	187.6	-1122.2	3	6	0.0	-	0	39	21	0.675	16	-23.7	15	0.682
83	-504.2	-631.5	3	6	46.1	-	0	31	10	0.603	58	-24.6	42	0.622
84	714.1	-1261.6	3	5	24.9	-	0	41	40	0.622	17	-23.1	14	0.621
86	-361.0	1518.4	3	6	36.5	+	0	4	40	0.710	25	-23.9	14	0.682
89	-71.8	-1691.6	3	6	17.3	-	0	48	50	1.324	7	-23.3	6	1.347
91	1474.0	-640.2	3	4	34.2	-	0	31	19	0.831	13	-23.5	13	0.831
92	472.1	-1666.4	3	5	41.0	-	0	48	25	0.753	19	-23.3	10	0.705
97	-534.1	-1286.2	3	6	48.1	-	0	42	5	0.542	9	-22.6	6	0.566
103	-1005.8	1200.3	3	7	19.5	-	0	0	38	0.700	6	-22.4	6	0.700
110	-362.2	1479.8	3	6	36.6	+	0	4	1	0.975	8	-23.2	7	0.967
111	649.7	-1062.1	3	5	29.2	-	0	38	21	0.726	9	-22.9	8	0.729
115	941.1	540.1	3	5	9.7	-	0	11	38	0.719	8	-22.6	8	0.719
120	-700.6	645.2	3	6	59.2	-	0	9	53	0.874	12	-23.7	10	0.861
121	-432.2	-1317.9	3	6	41.3	-	0	42	36	0.811	12	-23.0	11	0.816
123	718.0	-929.2	3	5	24.6	-	0	36	8	0.745	19	-23.2	17	0.748
126	-810.0	-954.2	3	7	6.5	-	0	36	33	0.575	13	-23.0	11	0.585
131	5.1	319.9	3	6	12.1	-	0	15	19	0.566	11	-22.1	7	0.605
135	-1451.4	714.7	3	7	49.2	-	0	8	44	0.579	17	-24.0	7	0.609
137	175.9	-1714.0	3	6	0.8	-	0	49	12	1.398	8	-24.1	7	1.397
140	1208.8	1662.9	3	4	51.9	+	0	7	5	0.602	10	-22.5	9	0.611

Table 3. continued.

ID	X	Y	RA (J2000)			Dec (J2000)			$\langle z \rangle$	n_{gal}	$M_V(\text{tot})$	n_{gal} $\sigma_z \leq 0.15$	$\langle z \rangle$	
150	-1201.8	1549.6	3	7	32.6	+	0	5	11	1.661	14	-25.2	7	1.651
153	1016.8	-1297.7	3	5	4.7	-	0	42	16	0.735	8	-23.4	8	0.735
156	1176.7	-1047.2	3	4	54.0	-	0	38	6	0.765	8	-22.0	6	0.748
160	-739.7	-237.9	3	7	1.8	-	0	24	36	0.568	12	-23.6	10	0.583
166	-212.2	618.7	3	6	26.6	-	0	10	20	0.558	13	-22.8	8	0.585
170	-680.4	-843.0	3	6	57.8	-	0	34	41	0.527	12	-22.8	9	0.535
174	447.2	9.9	3	5	42.7	-	0	20	29	1.618	13	-24.2	6	1.552
222	-494.2	-613.8	3	6	45.4	-	0	30	52	0.944	7	-22.9	7	0.944
225	-346.3	-1086.8	3	6	35.6	-	0	38	45	0.582	8	-23.6	8	0.582
241	805.0	-1034.8	3	5	18.8	-	0	37	53	0.639	9	-23.0	8	0.635
257	-1348.1	-132.2	3	7	42.4	-	0	22	51	0.525	8	-22.7	6	0.533
390	192.6	-345.5	3	5	59.6	-	0	26	24	0.603	8	-22.6	7	0.613
397	-1286.0	-1040.7	3	7	38.2	-	0	37	59	0.717	6	-21.9	6	0.717
2	1211.2	-1192.1	3	4	51.7	-	0	40	30	1.202	11	-23.7	5	1.233
23	853.6	-1071.7	3	5	15.6	-	0	38	30	1.256	6	-22.5	3	1.291
32	-1283.1	-558.9	3	7	38.0	-	0	29	57	1.224	10	-23.1	4	1.294
34	-1115.9	-783.3	3	7	26.9	-	0	33	42	1.163	10	-22.8	2	1.063
38	1631.4	-1161.2	3	4	23.7	-	0	39	60	1.068	6	-22.3	3	1.011
43	488.1	687.8	3	5	39.9	-	0	9	11	1.077	10	-22.7	2	0.984
57	8.4	-1275.9	3	6	11.9	-	0	41	54	1.175	6	-23.0	5	1.196
73	425.4	-1416.5	3	5	44.1	-	0	44	15	1.250	12	-23.7	4	1.269
74	-332.1	1160.6	3	6	34.6	-	0	1	18	0.515	12	-22.3	3	0.485
76	1635.1	-1581.1	3	4	23.5	-	0	46	59	1.260	9	-23.5	5	1.282
85	37.6	1375.6	3	6	10.0	+	0	2	17	1.269	11	-23.8	5	1.300
101	1405.8	-880.6	3	4	38.8	-	0	35	19	1.178	8	-23.7	5	1.149
113	656.9	553.1	3	5	28.7	-	0	11	25	0.925	6	-22.8	5	0.899
127	799.2	-1593.8	3	5	19.2	-	0	47	12	1.296	7	-22.3	2	1.239
142	-602.7	-763.9	3	6	52.7	-	0	33	22	1.011	8	-22.3	2	0.955
151	1399.2	1358.8	3	4	39.2	+	0	2	0	1.634	6	-24.1	4	1.613
155	432.8	-1403.9	3	5	43.6	-	0	44	2	1.522	7	-23.5	3	1.447
157	-322.5	1581.2	3	6	34.0	+	0	5	43	0.529	8	-21.3	2	0.525
161	-137.1	1624.8	3	6	21.6	+	0	6	26	1.185	6	-23.1	4	1.217
162	855.6	-1712.3	3	5	15.4	-	0	49	11	1.264	8	-22.9	4	1.288
180	-342.4	-320.9	3	6	35.3	-	0	25	59	0.812	6	-22.2	4	0.810
189	1232.8	-927.8	3	4	50.3	-	0	36	6	1.426	6	-23.5	3	1.470
192	-1632.1	1596.6	3	8	1.3	+	0	5	58	0.869	6	-22.0	3	0.942
205	-336.7	1381.2	3	6	34.9	+	0	2	23	1.425	7	-24.0	3	1.507
214	-1409.0	1634.9	3	7	46.4	+	0	6	37	0.545	6	-20.7	1	0.614
224	-938.7	-663.8	3	7	15.1	-	0	31	42	0.523	9	-23.6	5	0.529
242	303.5	1105.4	3	5	52.2	-	0	2	13	1.742	7	-23.9	3	1.656
261	-782.4	-534.7	3	7	4.6	-	0	29	33	0.566	8	-22.6	5	0.589
264	-1214.5	1684.1	3	7	33.4	+	0	7	26	1.598	7	-23.8	3	1.632
267	-605.4	1256.1	3	6	52.8	+	0	0	18	1.610	11	-23.9	4	1.492
386	580.1	-1549.6	3	5	33.8	-	0	46	28	1.517	6	-22.8	1	1.489
475	-1054.2	1011.4	3	7	22.8	-	0	3	47	0.449	6	-21.2	4	0.411
28	505.0	-1731.4	3	5	38.8	-	0	49	30	1.113	8	-21.4	0	
42	-1642.1	1490.5	3	8	1.9	-	0	4	12	1.194	6	-22.4	0	
146	-508.4	-1425.5	3	6	46.4	-	0	44	24	0.544	6	-23.0	0	
172	490.0	-1611.7	3	5	39.8	-	0	47	30	1.797	6	-23.6	0	

Notes. The gnomonic positions X and Y refer to the pointing centre of $\text{RA(J2000)} = 3^{\text{h}}6^{\text{m}}12^{\text{s}}.48$ and $\text{Dec(J2000)} = -0^{\circ}20'38''$. $\langle z \rangle$ and n_{gal} give the average photometric redshift and the number of member galaxies. $M_V(\text{tot})$ is the total rest-frame magnitude in the Johnson V -band. The last two columns list the average redshift and number of galaxies for those members with an error in the photometric redshift of less than 0.15.

The first part of the table lists those candidates which have six or more member galaxies for the restricted photometric redshift errors. The second part gives those candidates who fall below the limit of 6 members in the restricted sample and the third section gives those candidates who do not have any member galaxy with a photometric redshift error less than 0.15.

mock sky data based on the Millenium simulation (Zatloukal et al. 2009).

5. First results

Our tools for the cluster search were developed and first applied to the 03hA-field. The search was restricted to objects with

$H < 21.5$ mag and yielded a list of 114 cluster candidates with redshifts between 0.45 and 1.8. A full presentation and discussion of their properties (including the cluster selection function following the lines of Zatloukal et al. 2009) will be given together with the other HIROCS-fields in a separate paper. We present in Table 3 the list of candidates. A histogram of the errors in photometric redshift is strongly peaked below 0.15. Thus

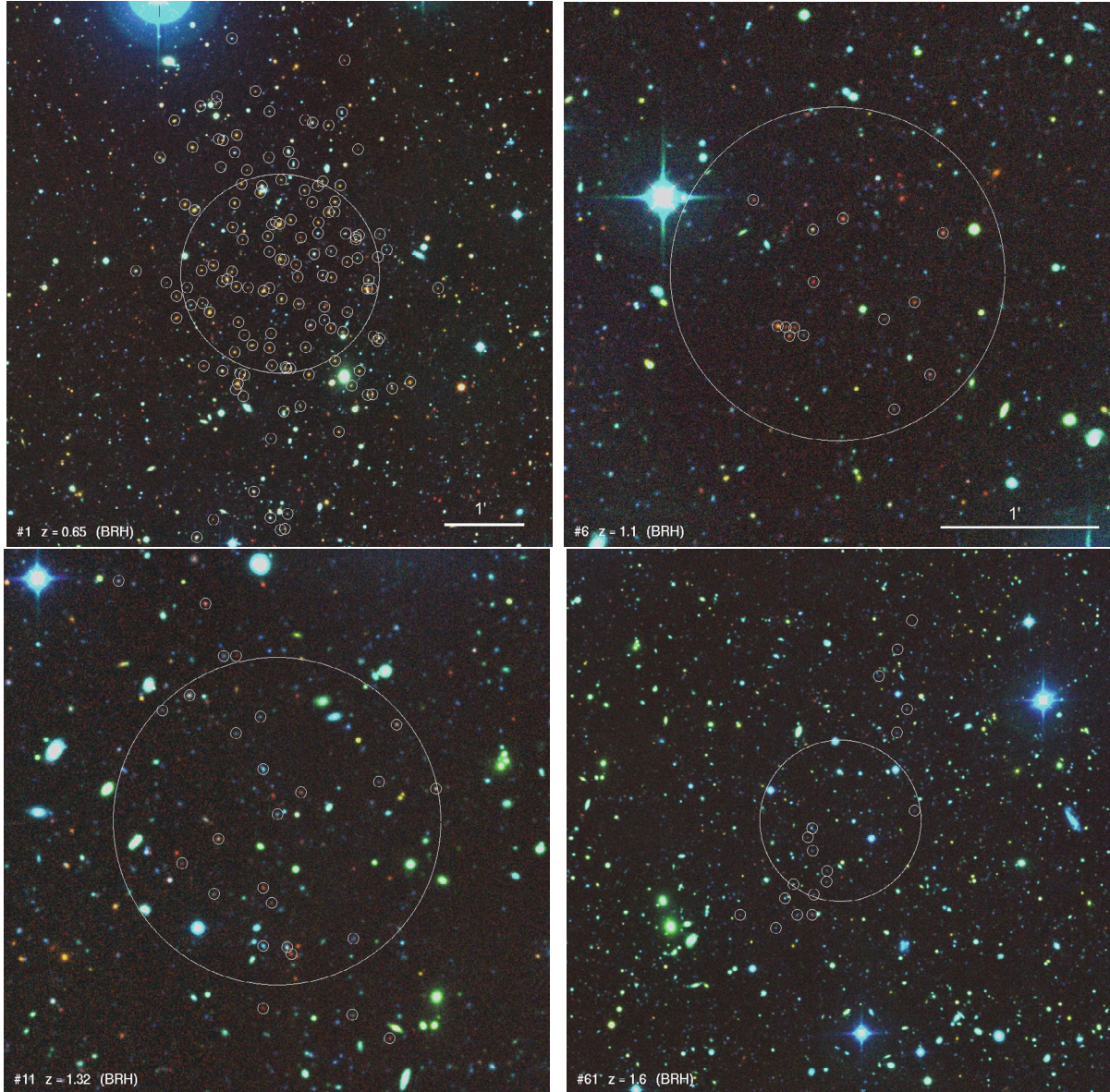


Fig. 15. False colour images based on the B , R , and H images of the four cluster candidates. Field size is $410''$ for *upper left* and *lower right* image, half that for the other. The circle represents 1 Mpc at the redshift of the cluster. *Top left:* candidate #1 at redshift $z = 0.65$ shows an excess of yellowish/red galaxies. *Top right:* candidate #6 at $z = 1.1$ has a majority of red galaxies. *Bottom left:* candidate #11 is at $z = 1.3$ with a larger fraction of blueish galaxies. *Bottom right:* candidate #61 has a high redshift of $z = 1.6$. The circle is centred on the original position of the 30 member galaxies selected by the FoF-algorithm. Restricting the member galaxies to those with $\sigma_z < 0.15$ reduces the number to 18 and shifts the cluster centre to the SE. All of the galaxies are blue.

the table is divided into three parts. First, the candidates are listed that after restriction to objects with redshift errors ≤ 0.15 still contain 6 or more member galaxies. These correspond to 78 clusters. For 4 candidates, no member galaxies were left after restricting the redshift error (last part of the table). Of the candidates in the first part 30 have a redshift below 0.7, 12 of which are below 0.6. According to Figs. 10 and 11, redshifts below 0.6 have a small chance to be at a much lower redshift around 0.2. However, only one of the candidates (#63) has an abnormally bright total absolute V -band magnitude because some stars and bright galaxies are included. Most of these 30 candidates are located in the central lower part of Fig. 14, which may suggest that here we probe part of a large-scale structure at redshift ≈ 0.6 .

For four candidates, more details are now provided to illustrate our results. These were selected from among the richest candidates to increase the probability of being real and are

indicated in Fig. 14 in colour. Their galaxy members were restricted to those with an error in the photometric redshift of less than 0.15, which is slightly above the median of the error distribution. For each cluster, a colour composite derived from the B , R , and H images is given in Fig. 15, histograms of the redshift distribution in Fig. 16, rest-frame colour–magnitude diagrams in Fig. 17, and representative spectral energy distributions in Fig. 18.

In Fig. 14, a very prominent cluster is evident at $X, Y = [1200, -750]$. It was already evident in the H -band sum image during data reduction as an overdensity of objects. It consists of 175 member galaxies (136 with redshift errors < 0.15) at an average redshift of 0.65. The galaxies are loosely distributed without any central concentration and no central brightest cluster galaxy is clearly evident. Its rest-frame colour–magnitude diagram shows a clear separation in a red sequence, which is about

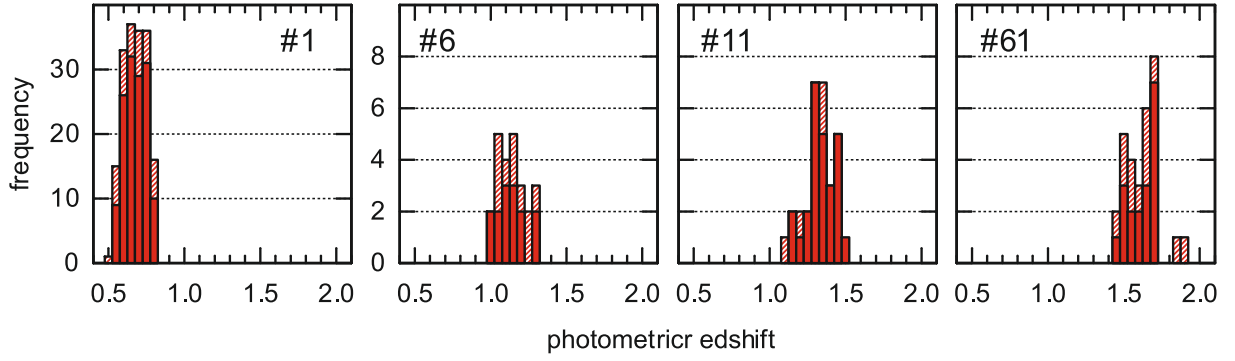


Fig. 16. Redshift histograms for the four cluster candidates. Dashed bins are for all objects allocated to the cluster, filled bins are restricted to galaxies with errors in the photometric redshift of less than 0.15.

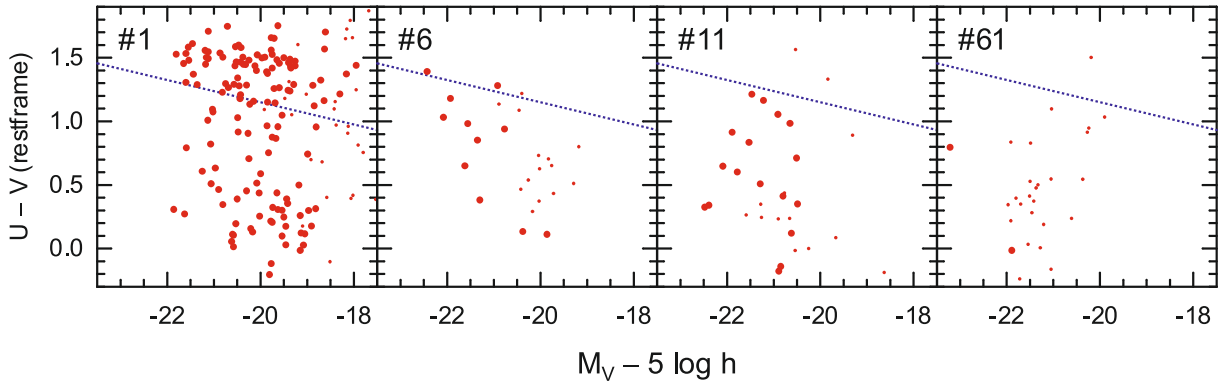


Fig. 17. Rest-frame colour-magnitude diagrams $U - V$ vs. V . Large dots represent member galaxies with an error in the colour less than 0.02 , other members are plotted with small dots. A progressively bluer population is seen as the redshift increases. For the lowest redshift candidate, a clear separation into red-sequence and blue-cloud is evident. At the highest redshift, no red-sequence is visible. The location of the red sequence determined by Bell et al. (2004) is indicated by the dashed line.

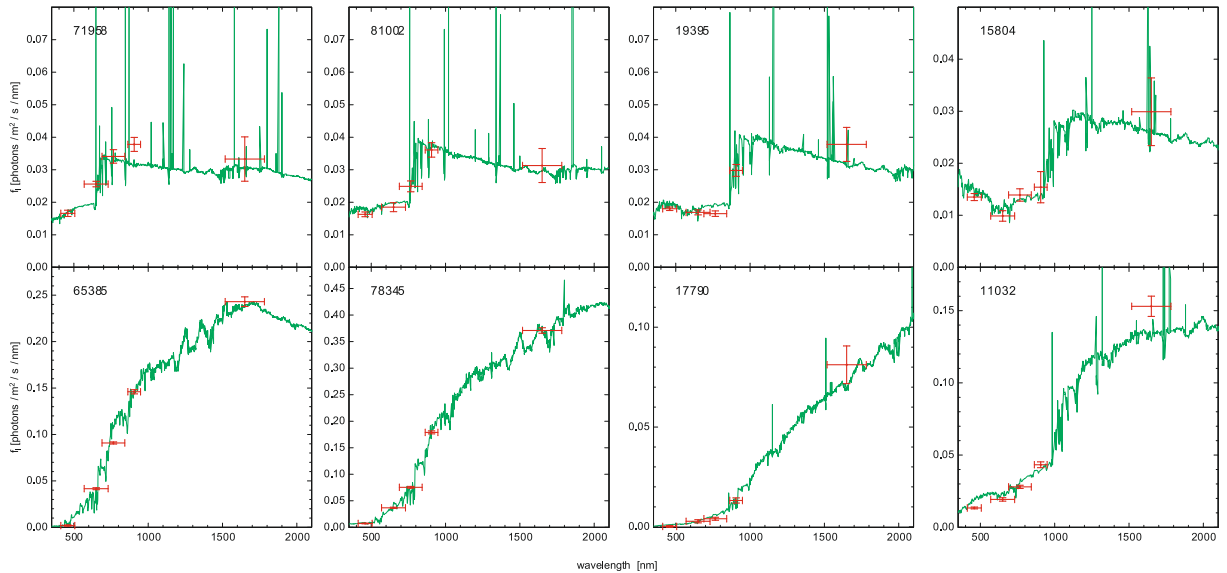


Fig. 18. Spectral energy distribution of galaxies from the cluster candidates. Displayed are one of the bluest (*top*) and reddest (*bottom*) cluster members for each candidate from low (*left*) to high (*right*) redshifts.

0.02 redder than the sequence determined for this redshift by Bell et al. (2004), and a blue cloud. The locations of red-sequence and blue cloud for this cluster candidate are identical to the location derived in Zatloukal et al. (2007) for the field galaxies in the COSMOS field in this redshift range.

Two cluster candidates are at intermediate redshifts, #6 at $z = 1.1$ and #11 at $z = 1.3$ (both just outside the redshift range

of high uncertainty, cf. Fig. 10), another one at the high redshift of 1.6. Restricting the cluster members to those with redshift errors below 0.15, the number of members found are 14, 26, and 18, respectively. The colour-magnitude diagram at the highest redshift shows only blue galaxies with no indication of a red sequence. This trend of an increasing fraction of blue galaxies with redshift can also be seen in Fig. 18, which shows the SEDs of

representative members. None of the clusters could be identified with an X-ray source in the ROSAT All-Sky Survey. The field is not covered by any XMM-Newton or Chandra pointing.

Once the selection function of HIROCS has been analysed in a similar manner to the simulations performed by Zatloukal et al. (2009) for the COSMOS-field using the Millenium simulation, the full HIROCS sample will be an ideal tool for studying the evolution of galaxy populations in distant clusters as a function of redshift and environment. The sample will also have to be compared to clusters drawn from X-ray surveys or those using IR-data from Spitzer (e.g., Eisenhardt et al. (2008)).

6. Summary

The multi-colour survey HIROCS utilises novel approaches for astrometric and photometric calibration of CCD mosaics. Its first application to a 3D-search for high-redshift clusters of galaxies in a 1° has identified a sample of 114 clusters, four of which are presented here in some detail to demonstrate the feasibility of the HIROCS approach. The complete sample of cluster candidates drawn from HIROCS over 8° will be presented in a separate paper. Follow-up observations with LUCIFER at the LBT are planned to verify representative candidates. The long-term goal of the survey is to supply a homogenous cluster sample selected solely on the basis of local galaxy density over the redshift range 0.8–1.5 to study the evolution of galaxies in clusters as a function of redshift and local density.

Acknowledgements. The authors thank the staff on Calar Alto and La Silla for their support with the observations and for performing part of the observations in service mode. We are grateful to René Faßbender for making his O2k pipeline available, to Georg Feulner for providing the MUNICS redshifts and to Kris Blindert for help with part of the LAICA observations. MZ kindly acknowledges support from IMPRS. C.W. was supported by an STFC Advanced Fellowship. For the overall project the use of the Digital Sky Survey, the NASA Extragalactic Database (NED) and the Astrophysics Data System (ADS) were of invaluable help.

This publication makes use of data products from the Two Micron All Sky Survey (2MASS), the Sloan Digital Sky Survey (SDSS) and the COSMOS data base. We thank these teams for their efforts, without which this work would not have been possible.

References

- Andreon, S., Willis, J., Quintana, H., et al. 2004, MNRAS, 353, 353
 Bailer-Jones, C. A. L., Bizenberger, P., & Storz, C. 2000, in Optical and IR Telescope Instrumentation and Detectors, ed. M. Iye, & A. F. M. Moorwood, SPIE, 4008, 1305
 Bartelmann, M., & White, S. D. M. 2002, A&A, 388, 732
 Bell, E. F., Wolf, C., Meisenheimer, K., et al. 2004, ApJ, 608, 752
 Bertin, E., & Arnouts, S. 1996, A&ASS, 117, 393
 Blakeslee, J. P., Franx, M., Postman, M., et al. 2003, ApJ, 596, L143
 Borgani, S., & Guzzo, L. 2001, Nature, 409, 39
 Botzler, C. 2004, Ph.D. Thesis, Ludwig-Maximilians-Universität, München, Finding structures in photometric redshift surveys, http://edoc.ub.uni-muenchen.de/2218/1/Botzler_Christine.pdf
 Butcher, H., & Oemler, Jr., A. 1984, ApJ, 285, 426
 de Propriis, R., Stanford, S. A., Eisenhardt, P. R., Dickinson, M., & Elston, R. 1999, AJ, 118, 719
 Dressler, A., A. Oemler, J., Couch, W. J., et al. 1997, ApJ, 490, 577
 Drory, N., Feulner, G., Bender, R., et al. 2001, MNRAS, 325, 550
 Eisenhardt, P. R. M., Brodwin, M., Gonzalez, A. H., et al. 2008, ApJ, 684, 905
 Elston, R. J., Gonzalez, A. H., McKenzie, E., et al. 2006, ApJ, 639, 816
 Falter, S. 2006, Ph.D. Thesis, Ruprecht-Karls-Universität Heidelberg, <http://www.ub.uni-heidelberg.de/archiv/6789>
 Faßbender, R. 2003, Diploma Thesis, Ruprecht-Karls Universität Heidelberg
 Faßbender, R. 2007, Ph.D. Thesis, Ludwig-Maximilians-Universität München
 Feulner, G. 2004, Ph.D. Thesis, Ludwig-Maximilians-Universität München
 Fruchter, A. S., & Hook, R. N. 2002, PASP, 114, 144
 Gabasch, A., Goranova, Y., Hopp, U., Noll, S., & Pannella, M. 2008, MNRAS, 383, 1319
 Gioia, I. M., Henry, J. P., Mullis, C. R., et al. 2001, ApJ, 553, L105
 Gladders, M. D., & Yee, H. K. C. 2000, AJ, 120, 2148
 Gonzalez, A. H., Zaritsky, D., Dalcanton, J. J., & Nelson, A. 2001, ApJ&SS, 137, 117
 HITRAN 2005, J. Quant. Spectr. Rad. Trans., 96, 139
 Ilbert, O., Capak, P., Salvato, M., et al. 2009, ApJ, 690, 1236
 Koch, A., Odenkirchen, M., Grebel, E. K., & Caldwell, J. A. R. 2004, Astron. Nachr., 325, 299
 Kovács, Z., Mall, U., Bizenberger, P., Baumeister, H., & Röser, H.-J. 2004, in Astronomical Telescopes and Instrumentation, ed. J. D. Garnett, & J. W. Beletic (Glasgow: SPIE – The International Society for Optical Engineering), SPIE Proc. Ser., 5499, 432
 Li, I., & Yee, H. 2008, AJ, 135, 809
 Lilly, S. J., Fèvre, O. L., Renzini, A., et al. 2007, ApJS, 172, 70
 Manfroid, J., Selman, F., & Jones, H. 2001, The Messenger, 104, 16
 Meisenheimer, K., Beckwith, S., Fockenbrock, H., et al. 1998, in The Young Universe: Galaxy Formation and Evolution at Intermediate and High Redshift, ed. S. D’Odorico, A. Fontana, & E. Giallongo (San Francisco: ASP), ASP Conf. Ser., 146, 134
 Meisenheimer, K., & Röser, H.-J. 1987, in The optimization of the use of CCD detectors in astronomy, ed. J.-P. B. D’Odorico, & S., ESO Conference and Workshop Proc., Garching, 227
 Meisenheimer, K., & Röser, H.-J. 1993, in Landolt-Börnstein Group VI, Landolt-Börnstein, ed. H. Voigt (Berlin – Heidelberg – New York: Springer Verlag), 3, 29
 Oemler, A., J., Dressler, A., & Butcher, H. R. 1997, ApJ, 474, 561
 Oke, J. B. 1990, AJ, 99, 1621
 Pickles, A. 1998, PASP, 110, 863
 Postman, M., Lubin, L. M., Gunn, J. E., et al. 1996, AJ, 111, 615
 Ramella, M., Biviano, A., Boschin, W., et al. 2000, A&A, 360, 861
 Rosati, P., Borgani, S., & Norman, C. 2002, ARA&A, 40, 539
 Röser, H.-J., Hippelein, H., & Wolf, C. 2004, in Clusters of galaxies: Probes of cosmological structure and galaxy evolution, ed. J. S. Mulchaey, A. Dressler, & J. Oemler, Augustus (Pasadena: Carnegie Observatories), Carnegie Observatories Astrophys. Ser., 3
 Röser, H.-J., & Meisenheimer, K. 1991, A&A, 252, 458
 Scodeggio, M., Olsen, L. F., da Costa, L., et al. 1999, A&AS, 137, 83
 Skrutskie, M. F., Cutri, R. M., Stiening, R., et al. 2006, AJ, 131, 1163
 Stanford, S. A., Eisenhardt, P. R., Brodwin, M., et al. 2005, ApJ, 634, L129
 Trevese, D., Castellano, M., Fontana, A., & Giallongo, E. 2007, A&A, 463, 853
 van Breukelen, C., Clewley, L., Bonfield, D. G., et al. 2006, MNRAS, 373, L26
 van Breukelen, C., Cotter, G., Rawlings, S., et al. 2007, MNRAS, 382, 971
 van Dokkum, P. G., Franx, M., Fabricant, D., Illingworth, G. D., & Kelson, D. D. 2000, ApJ, 541, 95
 Voit, G. M. 2005, Rev. Mod. Phys., 77, 207
 Wolf, C., Meisenheimer, K., & Röser, H.-J. 2001, A&A, 365, 660
 Wolf, C., Meisenheimer, K., Rix, H.-W., et al. 2003, A&A, 401, 73
 Wolf, C., Meisenheimer, K., Kleinheinrich, M., et al. 2004, A&A, 421, 913
 York, D. G., Adelman, J. J. E., Anderson, J., et al. 2000, AJ, 120, 1579
 Zatloukal, M. 2008, Ph.D. Thesis, Ruprecht-Karls-Universität Heidelberg, <http://www.ub.uni-heidelberg.de/archiv/8800/>
 Zatloukal, M., Röser, H.-J., Khochfar, S., et al. 2009, A&A, submitted
 Zatloukal, M., Röser, H.-J., Wolf, C., Hippelein, H., & Falter, S. 2007, A&A, 474, L5